JOURNAL OF AIRCRAFT
Vol. 48, No. 1, January–February 2011

Experimental and Computational Evaluation of Small Microcoaxial Rotor in Hover

Z. Liu*
University of Toulouse, 31400 Toulouse, France
R. Albertani†
University of Florida, Gainesville, Florida 32611
J. M. Moschetta‡
Institut Supérieur de l'Aéronautique et de l'Espace, 31055 Toulouse Cedex 4, France
C. Thipyopas§
Kasetsart University, 10900 Bangkok, Thailand
and
M. Xu¶
Northwestern Polytechnical University, 710072 Xi'an, People's Republic of China

DOI: 10.2514/1.C031068

An experimental and computational study of the static performance of small microcoaxial twin rotors with a diameter of 7.5 cm and twisted blades within Reynolds range from 6000 to 15,000 at 75% span was carried out. A test bench, which is based on five-component sting balance with maximum load capacity of 2 N, was designed. The sting balance experimental validation, carried out before the tests, showed average relative errors of forces and moments were 1.589 and 3.777%, respectively. Loading–unloading tests showed a relatively important hysteresis for low loads and a negligible hysteresis for higher loads. The static performance of the coaxial rotor was measured at three rotor axial stations, which are located 0.53, 1.07, and 1.60*R* from the center, with the maximum thrust at the middle station. A thrust of 0.112 N was measured at 6500 RPM for both rotors. The computational fluid dynamics solver Fluent was used in simulations. Flow models, such as laminar, Spalart–Allmaras, standard *k*-*ω*, and shear stress transport *k*-*ω*, were compared with different grid configurations. Results show that laminar model has the best fidelity for flowfield. Full simulations of the final coaxial rotor were performed with laminar model showing an overestimation of thrust and torque.

Nomenclature

A = rotor disk area, m^2
C_T = rotor thrust coefficient, $2T/[\rho_\infty A(\Omega R)^2]$
$\bar{c}$ = mean chord, m
FM = figure of merit of rotor, $C_T^{3/2}/(2C_Q)$
L = rolling moment, N · m
M = pitching moment, N · m
N = yawing moment, N · m
N_b = number of blades
Pre = precision of measurement
Q = rotor torque, N · m
Q_m = rotor torque coefficient, $2Q/(\rho A\Omega^2 R^3)$
R = rotor radius, m
Re = Reynolds number at 75% span of downstream rotor, $0.75\Omega Rc_{0.75}/\nu$
T = rotor thrust, N
T_m = collective thrust measured at a certain input pulse width modulation, N
$t_{v,P}$ = student t estimator given at probability P%, and a freedom of v.
v = degrees of freedom
Y = side force, N
Z = normal force, N
α = rotation angle, °
β = inclination angle, °
ε_q = quantization error of the acquisition system, N or N · m
ε_t = error of measurement in a subconfiguration, N or N · m
$\varepsilon_{\mathrm{Rel,total}}$ = relative error of measurement in all subconfigurations
φ = yaw angle, °
σ = rotor solidity, $N_b\bar{c}/(\pi R)$
ρ_∞ = freestream fluid density, kg/m^3
Ω_m = means of rotational velocity measured, rad/s

I. Introduction

MICRO Air Vehicles (MAVs) have achieved a great development in the past decade [1–5]. Nano air vehicles (NAVs) [6] proposed by the Defense Advanced Research Projects Agency (DARPA) in 2006 attracts more attention in recent years to fulfill missions in complex and cluttered environments. Various NAV concepts have been developed [7–9]. Coaxial rotor configurations process the advantages of compactness and high payload-carrying ability within the size and weight constraints. The configuration is therefore used to design NAVs in ISAE-SUPAERO (Institute Supérieur de l'Aéronautique et de l'Espace), even though the system of two rotors mounted in-line to each other increases the mechanical complexity and introduces the aerodynamic interferences.

Received 16 April 2010; revision received 16 August 2010; accepted for publication 17 August 2010.

*Ph.D. Candidate, International Joint Doctoral Program Between ISAE and NPU. Currently, Department of Astronautics, Northwestern Polytechnical University, 710072 Xi'an, People's Republic of China; liuzhen8191@gmail.com.

†Research Assistant Professor, Research and Engineering Education Facility; ralb@ufl.edu.

‡Professor, Department of Aerodynamics, Energetics and Propulsion; jean-marc.moschetta@isae.fr.

§Lecturer, Department of Aerospace Engineering; fengcpt@ku.ac.th.

¶Professor, Department of Astronautics; xumin@nwpu.edu.cn.

Furthermore, the in-line counter-rotating rotor enables a robust control of the torque, a potential problem for very small air vehicles.

The hover power requirement is the main difficulty in achieving a better performance for coaxial rotors since hover flight state has a typical low mechanical efficiency thus consuming a considerably large amount of energy. With the reduction of size and rotational velocity, nanocoaxial rotor operates in a significantly low Reynolds number range between 5000 and 15,000 accompanying with the phenomena of separation, transition and reattachment. The maximum figure of merit (FM) of micro rotor could drop to 0.2 [10,11] as a result, while full-scale helicopter has a maximum FM up to 0.8 [12]. Research on the aerodynamic and propulsion performance of coaxial rotors is considered critical despite the fact that the thrust and the torque of the rotors are significantly small in the order of 0.010 N and 0.001 $\mathrm{N \cdot m}$, respectively, due to the dimension and mass they represent critical parameters for a typical NAV. Coupling between torque and thrust makes the measurement sensitive to the test fixtures. Therefore, measuring both thrust and torque simultaneously is a significant challenge. It was noted by Mueller [13] that sensitive equipment must be used to perform aerodynamic measurements on small models at very low Reynolds numbers. To achieve this goal, a new aerodynamic balance was designed procured by ISAE-SUPAERO. Techniques to reduce experimental noise and increase the accuracy of the results were investigated by Mueller [13] and Albertani et al. [14] giving a special emphasis to the relevant noise-to-signal ratio using statistical techniques associated to a robust design of experiment (DOE). Bohorquez [15] and Bohorquez et al. [16] developed a stand with load cell and torque sensor to test the static performance of microcoaxial rotor of rectangle and tapered blades with diameters of 11.2 cm. A maximum thrust of 180 g was achieved, which is 1 order of magnitude larger than that of nanocoaxial rotor. The design and measurement of a gearless torque-canceling nanocoaxial propeller mechanism were conducted by measuring torque and thrust separately [9,17]. A maximum thrust of 17.28 g was measured. Relevant researches [18,19] have been carried out on static performance of small rotors and propellers. However, in these prior studies, the rotational speed and rotor diameter were larger than what is required for the NAV range.

For the coaxial rotor system, the flowfield is more complicated than that of single rotor due to the interaction between two rotor wakes. The wake effect is prominent and the phasing of the impingement of the tip vortex from upstream rotor upon the downstream rotor plays a significant role in the amount of unsteadiness on the downstream rotor [20]. And significant blade to vortex and vortex to vortex interactions is found for coaxial rotors. The tip vertex of upstream rotor interacts with the flow of downstream rotor. Computational methods are the useful way to study the coaxial rotor flow characteristics. Rotary-wing NAVs typically fly in the Reynolds number range from 10^3–10^4 where viscous effect is very strong; therefore, Euler equations frequently used for full-scale helicopters numerical study [21,22] are usually not applicable. In [23–25], compressible Reynolds averaged Navier–Stokes (RANS) equations with Spalart-Allmaras (S-A) model for rotary-wing MAV was adopted at tip Reynolds number varying from 19,000 to 27,000. It is found that thrust and power were reasonably predicted. Because the laminar flow is dominant when the Reynolds number is below 20,000 [26], the application of turbulence fluid model in the entire flowfield is still an opening debate to the simulation of rotary-wing NAVs. Because the coaxial rotors simulation involves two counter-rotating rotors at high rotational speeds, how to define rotor movement is a key problem. Chimera grids [27,28], sliding mesh [29], and multiple reference frame (MRF) [30] techniques are widely used to solve this problem.

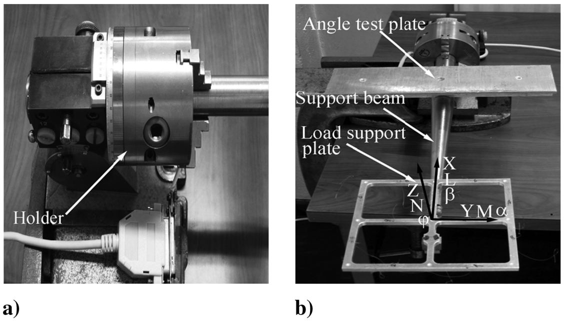

Fig. 1 Fixture for sting balance: a) lateral view, b) top view.

Studies of coaxial rotor with twisted blades in a low Reynolds number range of less than 15,000 are limited. For a deep understanding of the performance of such small rotor, a test bench based on a 2 N five-component sting balance is designed to measure small forces and moments simultaneously. Because the balance will be applied to measure very small forces and moments, evaluation of the balance is extremely important to present the characteristics of test facilities. Calibration methods of strain-gage balances have been well developed to obtain the calibration matrix [31]. Validation of the calibration matrix with an acquisition system different from the balance's manufacturer is usually performed by the users [32–35], because the accuracy of the balance and acquisition system combined directly influence the accuracy of wind-tunnel result. An evaluation method was used to apply the loads on balance by rolling and pitching it to realize coupling among the forces and moments. Low loads between 0 and 20% of full load, and high loads, between 20 and 100% of full load, were tested to learn the overall performance of the balance used in this work. Measurement error and precision of the system were estimated, and the hysteresis property of the balance was evaluated as well. Having been validated, the balance was used to measure the static performance of the coaxial rotor. Special supporting beams were fabricated to fix the rotor and corresponding electronic system on the balance. A 0.5 N beam load cell was installed on the balance to measure thrust of one rotor. A removable beam is used to adjust rotor spacing to verify its influence on rotor performance. A numerical simulation was also carried out and compared with experimental results. Ansys-Fluent [36] as a well-developed commercial computational fluid dynamics (CFD) code incorporates various flow models and computational methods. It is verified to be capable of simulating static mixers with helical elements.** Computations are carried out with laminar flow model and several turbulence models including S-A, standard k-ω model, and shear stress transport (SST) k-ω model using different element discretization schemes, to verify the influence of flow model and grid configurations on computational results. MRF method is applied to define the movement of coaxial rotor.

II. Experimental Setup and Computation Methodology

A. Sting Balance Validation Setup

The main objective of this experiment is to assess the sensitivity and resolution of the newly acquired nano-sting balance. An internal force sting balance manufactured by l'Institut Aerotechnique in France was used as the main test element to measure the change of total thrust and torque varying with rotational velocity of both rotors. The five-component sting balance, which is able to measure thrust and torque simultaneously, has a maximum loading capacity of 2 N for forces (Z and Y) and 0.12 $\mathrm{N \cdot m}$ for moments (L, positive with right hand rule; M, positive with left hand rule; and N, positive with left hand rule). The structural component, made of high strength steel alloy, 35NCD16, has a maximum dimension of 40 mm with a 10 mm rectangular support part on both sides. Validation experiments were carried out using a PXI-1050 chassis requiring a set of custom-made hardware and software for the installation of balance, data acquisition, and postprocessing. A test procedure for the management of experiments, and the analysis method for result processing are specifically designed. The fine evaluation of the balance was possible by using a customized fixture consisting of a clamp, a supporting beam, a load-support plate and an angle-test plate, as illustrated in Figs. 1a and 1b. The clamp is settled on the table fixing the supporting

---

**Data available online at http://www.bakker.org/cfm [retrieved 12 Sept. 2009].

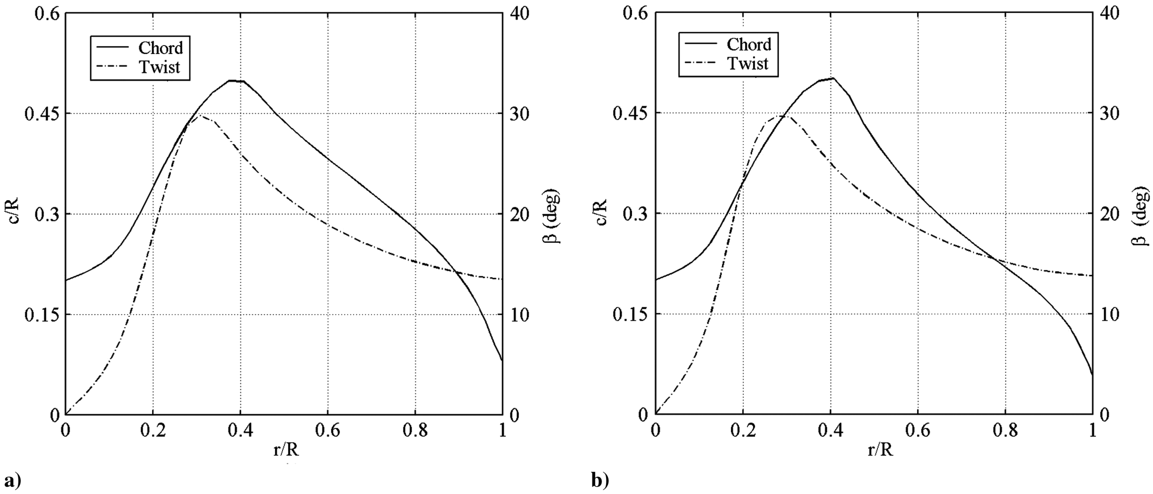

Fig. 2 Blades chord and twist distribution: a) upstream rotor, b) downstream rotor.

beam in a cantilevered position with pitch and roll degrees-of-freedom. One end of the beam is held by the clamp, and the other end is attached to the balance. On the supporting beam, an angle-test plate, with the same attitude as balance, is placed parallel to the load-support plate to place the protractor for angle measurement.

Because the error and accuracy depend on the bias between measured and real values, the determination of real values require high accuracy. The reference masses for load have been measured by high accuracy balance SARTORIUS, which has maximum capacity of 2 kg and accuracy of 0.0001 g [35]. The resolution and sensitivity of the entire acquisition system are critical for the validation of measurement accuracy. In this experiment, a PXI-1050 chassis, including SCXI-1520 signal conditioning unit, multifunction I/O-DAQ, NI PXI-6229 series 16-bits card and PXI-8336 interface was used as acquisition system. The SCXI-1520 module is an eight-channel module for interfacing to strain-gauge bridges and other Wheatstone-bridge-based sensors.[††] The SCXI-1520 signal conditioner supplies an excitation voltage of 4 ± 0.036 V to the balance during the experiment. Output signals from the balance are amplified by SCXI-1520 with a gain of 1,000 and filtered at 10 Hz.

Via a front module PXI-8336, the chassis is connected through an optical cable to a Dell Optiplex 330 PC with 1.98 GB RAM. The PC runs Measurement and Automation Explorer as driver interface between control software, LabView, and the PXI-1050. Customized Labview virtual instruments (VI) codes were developed for reading and displaying raw outputs (voltages) from the five channels and data logging. The VIs mainly contain the following functions: setting sampling frequency and number of samples to average for each channel, setting of the channel properties, and sting balance calibration matrices, display functions plotting forces and moments, input-output functions of measured data, input parameters of the experiment, real time of row-voltages, forces and moments for each channel on operator's screen.

A user interface was developed for further result process. It is based on the Graphical User Interfaces [37] programming tool of Matlab 2006a. It also includes error and confidence interval evaluation.

B. Coaxial Rotor Description

To solve the problem of significant propulsive performance degradation of nanopropellers due to its small size, ISAE aerodynamics and propulsion lab proposed a rotary-wing NAV concept with coaxial rotor. Such vehicle requires carrying a payload of about 0.02 N to meet DARPA's requirements [6]. Coaxial rotor has the advantages of compactness and high thrust compared with conventional concepts with same size. Conventional helicopter rotor typically has uniform chord. It controls attitude and flight direction through collective and cyclic pitch control [12]. Because small MAVs are characterized by extremely small size and weight, conventional controls are not feasible. Therefore, rotor blades with twisted and non uniform chord are particularly attractive for propulsion optimization. Thus a pair of nano counter-rotating rotors with diameters less than 7.5 cm was designed based on low Reynolds number aerodynamics and minimum induced loss theory [38,39] to minimize energy loss. The blade airfoil has 2% thickness with 5% curvature circular arc. In prior study [40], it was found that maximum motor mechanical efficiency occurs at about 6500 RPM for a 7.5 cm-diameter rotor; the concept design requires a total thrust of combined rotors larger than 0.10 N. Taking account of fabrication errors, the optimal design increases minimum total thrust to 0.120 N. The XROTOR code [41] was applied to optimize rotor geometries. Airfoil aerodynamic parameters at different Reynolds number were calculated before the optimization. With the potential formulation which is an extension of Goldstein's two and four blade solution to arbitrary numbers of blade and radial load distributions, the geometry of undisturbed upstream rotor can be obtained by defining the rotational velocity, thrust, and power consumed. The induced velocity was recorded as additional axial and rotational velocity components of freestream of downstream rotor. However, the interaction between rotors depends on their spacing and rotational direction. A rotor weight factor is therefore defined as the magnitude of the influence of the induced flow of the upstream rotor to the downstream rotor in terms of axial and tangential velocities. The product of weights and the components of induced flow plus the velocity of freestream are taken as the upstream flow velocity of downstream rotor. Because both rotors are counter-rotating with small spacing that is less than 2R, weights of 1.0 for axial velocity and −1.0 for tangential velocity are specified to reflect the influence of the upstream rotor induced velocity field to downstream rotor. By integrating the influence of upstream rotor and freestream condition, the downstream rotor geometry can be optimized with the rotational velocity, thrust and power as well. Similarly, the induced velocity of downstream rotor will influence the upstream as well. Its induced velocity will be taken into account to optimize the upstream rotor with weights of 0.5 for axial velocity and zero for tangential velocity specified. Solution converges after six iterations and there are no changes in chord length and twist angles. However, the rotors were optimized in a static condition which is thought to be a significant flight condition for NAVs. The chords lengths and twist angles at blade root for both rotors are too big to be fabricated. Modifications are therefore performed at blade root. In the end, an upstream rotor with mean chord of 0.33R and mean twist angle of 17.21° and a downstream rotor with mean chord of 0.31R and mean twisted angle of 17.67° were obtained (Fig. 2). Calculation of optimized rotors with XROTOR shows that the downstream and upstream rotor

---

[††] Data from the SCXI-1520 User Manual available online at http://digital.ni.com/manuals.nsf/websearch/74F442BE4AFE68EE8625707E006AE9D6 [retrieved 20 Aug. 2009].

generate a total thrust of about 0.127 N and zero torque during hovering at 6500 RPM for both rotors. After obtaining chord length and twist angle distribution, both rotors were to be fabricated. Because the rotors are thin and teetering, it is very hard to fabricate it with a machine. Conventional method was applied to fabricate them with two molds. Two 0.102 mm-thick carbon fiber layers and epoxy resin were used and the finished rotors are shown in Fig. 3. However, it should be pointed out that the thickness of rotors becomes nearly identical resulting in geometry difference between fabricated and optimized rotors.

C. Coaxial Rotor Experiments Setup

Because the reference center of measurement is located at the mechanical center of the sting-balance, beams with rectangular grooves were fabricated and fixed on the rectangular support end of the sting balance to secure rotor as illustrated in Fig. 4. To measure the thrust of both rotors, a beam load cell F1200 manufactured by MEIRI with a capacity of 0.5 N was used to measure the thrust of the downstream rotor. The thrust of the upstream rotor could be obtained by subtracting the thrust of the downstream rotor from total thrust. The total torque of the two rotors could be obtained from pitching moment component signal from the sting balance. A carbon support tube on which the upstream rotor was fixed could be adjusted to change the axial spacing between rotors thus the influence of the axial spacing between rotors could be studied. The LRK10-1-50Y motor from Wes-Technik that drives the rotor weights only 1.4 g. It is powered by a N5766A 3.7 V DC power supply by Agilent Technologies. The YGE4-BL from Wes-Technik Company controls the brushless motors. Optical sensors integrated with laser emitter and detectors are used to measure rotational speed of the motors. Ambient pressure and temperature sensors were applied as well for air density calculation.

During rotor tests the balance output signals were transferred to the PXI-1050 chassis for processing together with the rotational speed, and the input voltage and current and organized in the output file for further postprocessing.

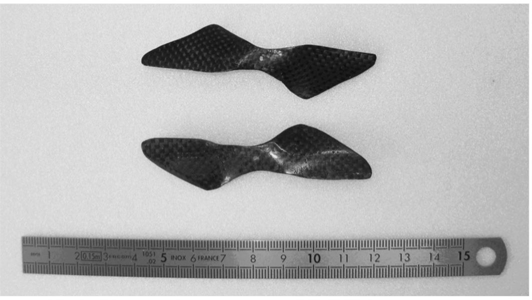

Fig. 3 Finished rotors.

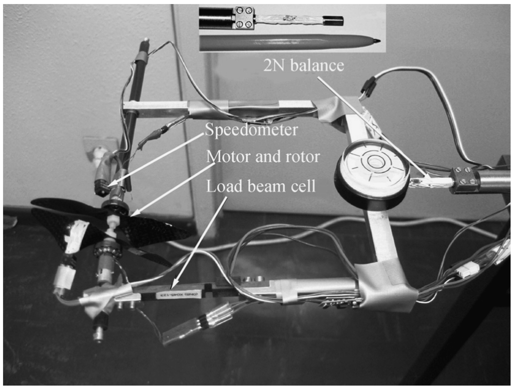

Fig. 4 Test bench and sting balance.

D. Computation Methodology

The numerical simulation was performed using FLUENT V6.3, a software package capable of solving Euler equations, RANS equations, or space-filtered equations. The conservation of mass, momentum, energy, and so forth, can be obtained using finite volume method.

A pressure-velocity coupling approach was used to improve solver robustness. Several spatial discretization schemes are provided by Fluent such as first-order upwind, second-order upwind, power law, QUICK and third-order MUSCL. In this study, the first-order upwind scheme and QUICK scheme were applied. First-order upwind scheme determines all the variables by assuming that the cell-center values of any variable represent a cell-average value and hold throughout the entire mesh. The QUICK scheme calculates higher-order value of convected variable at cell face by using a weighted average of second-order upwind and central interpolation. Laminar flow model was employed first. Several turbulence flow models were introduced later. S-A model, a single-equation conservation turbulence model provides good prediction of regular flows but fails to simulate flows with mild separation or circulation. The k-ω model solves two additional conservation equations in which one is for the turbulent kinetic energy k and the other is for the inverse time scale ω. Standard k-ω model is typically adopted for low-Re number or for transitional flows, while SST k-ω model is suitable for complex three-dimensional flows with strong rotation.

To modeling blade rotation, disk-actuator model, MRF technique or fully unsteady approaches such as sliding mesh method and chimera technique is frequently used. Disk-actuator model is a steady method which considers rotor as a disk where the induced velocity is specified without accounting for blade details. The MRF model [36] is a steady-state approximation in which individual cell zones use different frame equations to solve N-S equations. Zones containing moving components can then be solved using moving reference frame equations, whereas stationary zones can be solved with stationary frame equations. At the interfaces between cell zones, a local reference frame transformation is performed to enable flow variables in one zone to be used to calculate fluxes at the boundary of the adjacent one. If moving reference frame is used in a zone, the velocities and velocity gradients are converted from a moving reference frame to the absolute inertial frame whereas the scalar quantities are determined locally from adjacent cells, because these vector quantities change with reference frame. On the other hand, quantities in the absolute inertial frame can be converted to moving reference frame as well. Fully unsteady methods simulate blade motion by embodying the rotors in subzones in which its surrounding grids around move during computation. Disk-actuator model is the most time-saving method, but it depends on the precision of specified conditions for the disk and ignores the detailed blade geometry character. The fully unsteady methods allow one to simulate transient phenomena, for instance the vortex shedding from a rotating blade, but it requires several times' CPU-time than other methods. For this case with a steady rotating velocity, it is convenient to use MRF so that the steady-state solutions are possible with relatively short computing time and relatively high precision.

III. Experiment Design and Data Processing

A. Sting Balance Validation Design

The five-component sting balance represents the main source of output experimental data. Therefore, its accuracy was carefully evaluated before performing the counter-rotating nanorotor tests. A critical aspect of the sting balance characterization is the interactions between the axial and torque output signals. Such effects were simulated during the balance validation tests by rotating the balance around the X and Y axes illustrated in Fig. 1b. To simplify the notations for further postprocessing, the measurements performed at the same pitch and roll angles are defined as a configuration. For the sting balance standard validation tests, five configurations were performed. In each configuration, there are two subconfigurations including lower loads (between 0 and 20% of full load) and higher loads (between 20 and 100% of full load), respectively. To solve the

Table 1 Summary of applied forces and moments

Parameters	Load component	Y, N	Z, N	L, N·m	M, N · m	N, N · m
Normal tests	Maximum load	0.001	−0.0042	0.0918	0.1099	0.0858
	Minimum load	−0.730	−1.588	−0.0881	−0.0918	−0.0544
Hysteresis tests	Maximum load	0.0013	0	0.0965	0.0482	0.0858
	Minimum load	−0.7849	−1.5687	−0.0483	−0.0299	−0.0544
Balance	Capacity	±2.00	±2.00	±2.00	±0.12	±0.12

sting balance output signals the calibration matrix provided by the manufacturer was used for both load ranges. Within each subconfiguration, three different positions have been randomly chosen from the ten positions in the load support plate in Fig. 1b; at each position three different calibrated weights were applied in a random order. The measurements were repeated 5 times for each position and each weight recording 1000 samples for each measurement. The applied loads are summarized in Table 1. Because of the methodology used for the validation tests, the loads may not cover the entire range of the load capacity of the balance but would nevertheless provide a rather complete evaluation for the five components as required.

Furthermore the hysteresis property of the balance was evaluated including two configurations with different pitching and rolling angles at lower loads (between 0 and 10% of full load) and higher load (between 10 and 100% of full load). Within each configuration, two different positions have been randomly chosen on the apparatus plate and at each position a sequence of five weights were progressively loaded and unloaded repeating the measurement 5 times at each position. The applied loads are listed in Table 1.

B. Data Processing

The sting balance measurement precision is defined as the standard deviation of the force or moment for all acquisitions in a subconfiguration. The error is defined as the averaged differences between the applied and measured force/moment components for each test. And the relative error is defined as the ratio of averaged differences between the applied and measured force/moment components to the applied ones for each test.

During every coaxial rotor test, the variables are recorded for 15 times. For variables that are linear functions of the other independent variables directly measured, the mean value and standard deviation can be derived from measured values.

All of the results will have a confidence of 95% in the experiments.

C. Coaxial Rotor Experiment and Computation Design

The 0.5 N beam load cell is validated as well, but no detailed description will be presented here. In the study, the rotor spacings of 0.53, 1.07, and 1.60R are applied, respectively, to verify their influence on propulsive performance of counter-rotating rotors. The component Y of the sting balance is applied to measure the total thrust of coaxial rotors, while the 0.5 N beam load cell is used to measure the thrust of downstream rotor. The total torque of both rotors is measured by the component M of sting balance. The experiments were all carried out at a tension input to controller of 3.7 V which has the same value as the NAV battery. At each rotor spacing, the experiment was firstly carried out by fixing the rotational velocity of the upstream rotor at 6500 RPM, Reynolds number at 3/4R of 15,000, and changing downstream rotor rotational velocity with the input current from the Reynolds number of 6000–14,000. During the experiment, the rotational speed, input current, input voltage, and the thrust of each rotor were measured, but only the total torque was measured. Calculations are performed with laminar flow model and turbulence flow models using MRF method at a rotational velocity of 6500 RPM for both rotors. The spatial discretization schemes were also studied. Finally, the laminar flow model was used to simulate rotor spacing of 1.07R using MRF method.

IV. Results and Discussion

A. Sting Balance Validation Results

Considering the experimental methodology presented above, the validation of the setup was performed and the measurement precision and error were estimated. Different measurements with five configurations were performed including two subconfigurations for each configuration with loads between 0 and 20% of the maximum load and between 20 and 100% of the maximum load. All the results are calculated assuming a confidence of 95%. Figure 5 shows the plots of the measurement precision. The precision analysis shows that the maximum Pre is 0.0071 N for the forces and 0.000265 N · m for the moments. Furthermore, the component Y has higher maximum Pre than the Z component; the N component has the

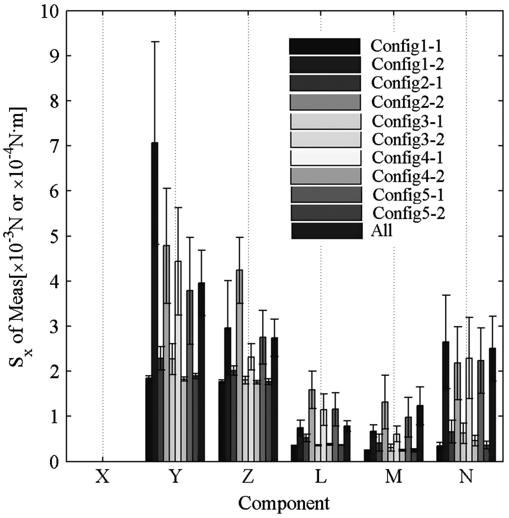

Fig. 5 Measurement precision; from left to right for a component, the columns are for Config1–1, Config1–2, and so forth, respectively.

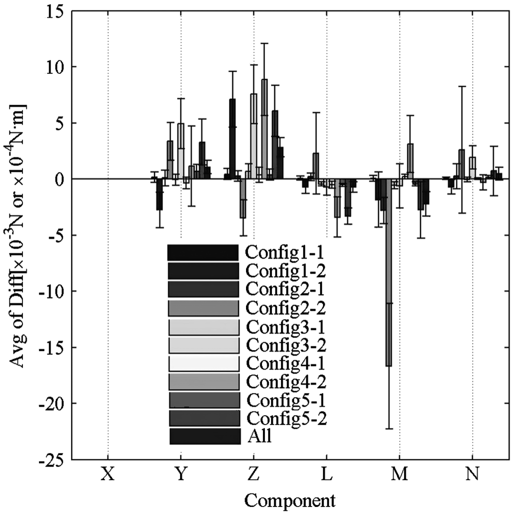

Fig. 6 Error plot: from left to right for a component, the columns are for Config1–1, Config1–2, and so forth, respectively.

Table 2 Relative error of 2 N balance

Components	Y, N	Z, N	L, N · m	M, N · m	N, N · m
Relative error	1.589 ± 0.337%	0.887 ± 0.137%	1.117 ± 0.192%	3.777 ± 1.463%	1.941 ± 0.442%

largest Pre of the three-moment components. The error of the measurement system consists of the error introduced by the sting balance, the mechanical and electronic components. Therefore, a maximum ε_t of 0.0088 N for the force and 0.00167 N · m for the moment were obtained (Fig. 6). The Z component has the maximum ε_t during the tests in which the roll angle and the pitch angle were coupled with a maximum load of 1.47 N (150 g) suggesting that the coupling of the two components may lead to an increase of the error. From Fig. 6, because ε_t depends on the loads, the relative error $\varepsilon_{\mathrm{Rel,total}}$ is introduced to present the performance of sting balance more clearly. The relative errors for the five components are listed in Table 2.

The maximum average relative error for all configurations, which is 3.777%, was found in the pitching moment component, although the minimum average relative error, assigned to the normal force component, is less than 1%. Generally, all the components have an average relative error less than 2%. The maximum average relative error was measured in the M component in the tests with a significant combined force and moment loads. Compared with the 1 kg maximum load balance from the University of Florida [30], whose ratio of accuracy to maximum load is less than 0.125% for all components, the sting balance seems to have a high relative error. However, the relative error calculated here is the ratio of absolute error to corresponding local load instead of maximum load. And the maximum loads of the two balances are different.

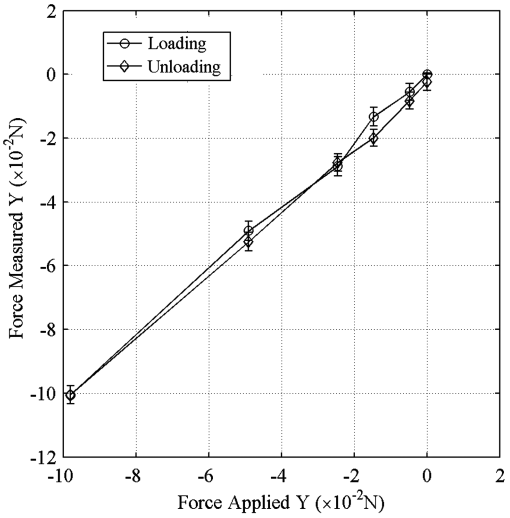

Fig. 7 Hysteresis property of component *Y*.

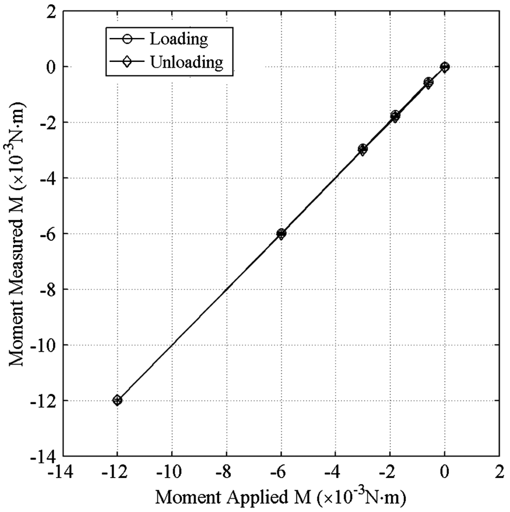

Fig. 8 Hysteresis property of component *M*.

The sting balance hysteresis characterization was also performed for all five components at the low load and high load range. From the hysteresis test results, it was found that the force components Y and Z (side and normal, respectively) and moment components L and N (roll and yaw, respectively) exhibited a mild hysteresis at the lower load range. The moment component M exhibited no significant hysteresis. For their significance for the presented static performance study of coaxial rotors, the hysteresis properties of the component Y and M at the low load range are illustrated in Figs. 7 and 8. The Y component (side force) was used to measure the total axial force of the coaxial rotors

Because the experimental results presented above are relative to the complete system, a careful check of all possible sources of errors must be included. The most important contributors of the validation system error was considered to be the measurement error of pitch and roll angles which were obtained by a digital protractor with a resolution of ±0.1°, positioned on the test plate illustrated in Fig. 1b. Great care was used for the positioning of the test plate on the sting balance to assure a proper alignment. It is believed that the magnitude of the loads and the value of the attitudes of the balance have an effect on the precision as well due to the increase of the coupling among the three moment components resulting in larger errors. Other potential sources of errors are the intrinsic high noise-to-signal ratio and the elastic deflections of the sting balance under load.

B. Rotor Performance Results

The calculations were performed at a rotors axial spacing of $1.07R$. The grid was generated using ICEM CFD V11.0. For the MRF method, the flowfield is divided into three volumes in which two small blocks are dedicated to the rotors, as shown in Fig. 9. The external mesh boundary is formed by a $25.5R$ high cylinder with the top and bottom radii of $12R$ and $16R$, respectively. Every small block has a height of $2/3R$ and a diameter of $1.5R$. Figure 4 shows that, each rotor is a solid thin piece of carbon fiber with twisted and nonuniform chord blades. Because the rotors were driven by external brushless motors, a small cylinder with the same diameter as the motor was added at the center of each rotor. The fine O-grid mesh,

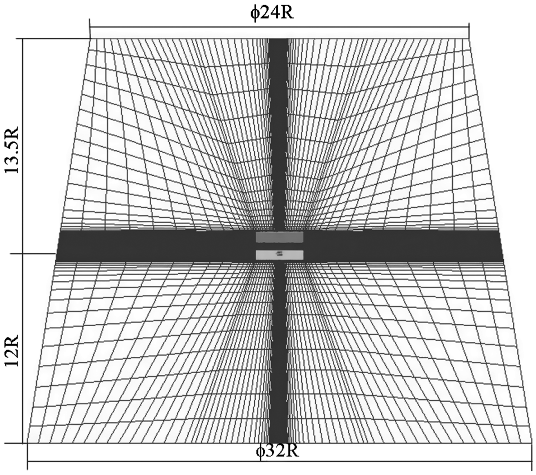

Fig. 9 Global view of the mesh.

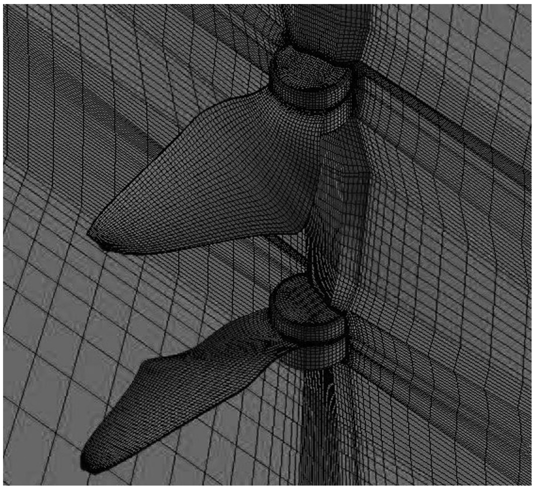

Fig. 10 Grid around blades.

shown in the Fig. 10, was defined and optimized around the rotors to capture the details of the flow structure and included a total number of grid cells of 2.8 Million.

Table 3 shows the thrust and torque calculated with different flow models and discretization schemes based on the MRF method at a rotational speed of 6500 RPM for both rotors and a rotor spacing of $1.07R$. The counter-rotating rotors were originally designed using XROTOR with the requirement for a total thrust of 0.127 N and zero torque. Both experimental and computational results show lower thrust and higher torque compared with the values predicted from XROTOR predictions. Furthermore, all the flow models used in the simulations overestimate the thrust and underestimate the torque when compared with the experimental results. If compared with the experiment, the turbulence model *k-ω* with the Quick scheme predicted the most accurate value for thrust with the first-order discretization scheme and the most accurate value of torque. Because the Quick discretization scheme introduces small truncation error, the absolute values of thrust and torque predicted by the simulations are slightly higher than first-order method except S-A flow model. In general, differences among computational results are considered negligible. When comparing the experimental with computational results, a relatively good agreement for the thrust and an underestimation for torque were found.

Because the fidelity of the performance prediction of rotors in static conditions is greatly influenced by the ability to capture tip vortex structure and the related disturbed flowfield, a detailed visual comparison of the flowfield between laminar and *k-ω* models with Quick scheme was conducted, as illustrated in Figs. 11 and 12. Figure 11 shows the pressure contours on the suction side of the blades for both rotors. It is evident that laminar model captures disturbance of flowfield near the blade tip while *k-ω* model fails. The blade tip vortex flowfield is extremely complicated, with the presence of secondary vortices near the tip increasing the complexity and the pressure distribution, as illustrated in Fig. 12. The secondary vortices can be clearly observed from calculated results obtained with the laminar model (Fig. 12a). Figure 12b shows that the turbulence *k-ω* model only predicts weak secondary structures validating the assumption that the laminar flow dominates the flowfield at the extremely low *Re* numbers even though strong flow interactions exist between the two rotors. It is postulated that the turbulence flow model failed to precisely predict the flowfield mainly because of its application on the entire volume without considering the transition. Furthermore it was found that at a short distance from the blade's trailing edge the secondary vortices merge with the tip vortex.

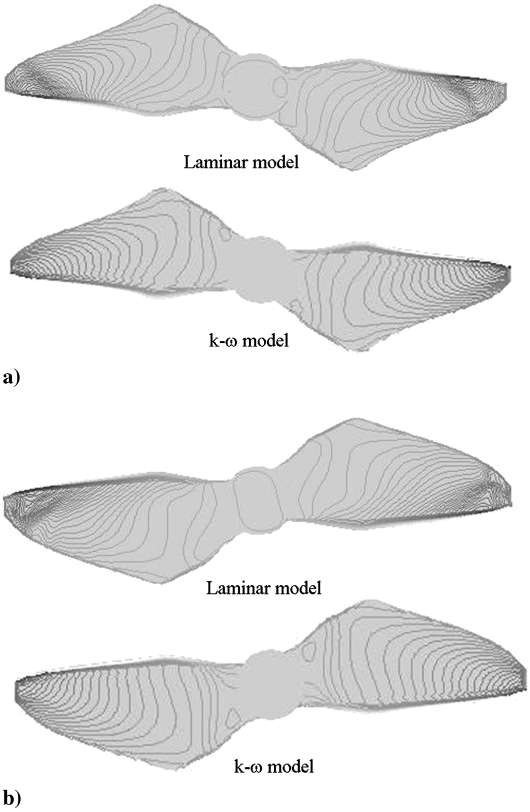

Fig. 11 Comparisons of computed pressure contours using different flow models: a) upstream rotor, and b) downstream rotor.

Figure 13 illustrates the experimental and calculated total thrust and torque of both rotors with the Reynolds number at $3/4R$ of the downstream rotor as an independent variable. Simulations were performed with the laminar flow model and Quick scheme at rotor axial spacing of $1.07R$, while the experiments were conducted at rotor axial spacings of 0.53, 1.07, and $1.60R$. The total thrust increases with the Reynolds number and peaks at $1.07R$, whereas Bohorquez's study [15] shows that the system thrust does not undergo measurable changes at vertical separations larger than $0.4R$. Differences less than 0.017 N were found between experimental and computational results. Experimental total thrust of 0.135 N was obtained at a *Re* number of about 14,000. A total thrust of 0.112 N was obtained from the experiment while a value of 0.121 N from the simulation at 6500 RPM for both rotors. However, both results were found smaller than XROTOR estimation. At same rotors tip speeds, absolute values of from both experiment ($4.918\mathrm{E}-04\ \mathrm{N}\cdot\mathrm{m}$) and simulation ($8.2\mathrm{E}-05\ \mathrm{N}\cdot\mathrm{m}$) are both larger than XROTOR prediction (zero). Comparing the experimental and computational results a larger difference was found for the torque than for thrust; both differences are fairly constant with Reynolds number. During the experiments, the downstream and upstream flow of the rotors experienced a certain blockage by blade speed sensors, the load cell and supporting beams influencing the performances of the rotors. Moreover, the average relative errors obtained from the sting balance validation tests for the components *Y* (thrust) and *M* (torque) of sting

Table 3 Comparison of experimental results and computational results calculated with different flow models

Flow model		Experiment	XROTOR	Laminar	S-A	*k-ω*	*k-ω* SST
First order	Total thrust, N	0.1120	0.1270	0.1209	0.1199	0.1194	0.1211
	Total torque, $\mathrm{N}\cdot\mathrm{m}\times10^{-3}$	−0.4918	0	−0.02840	−0.03530	−0.0746	−0.0168
Quick	Total thrust, N	0.1120	0.1270	0.1282	0.1199	0.1206	Not converged
	Total torque, $\mathrm{N}\cdot\mathrm{m}\times10^{-3}$	−0.4918	0	−0.08044	−0.03532	−0.09320	Not converged

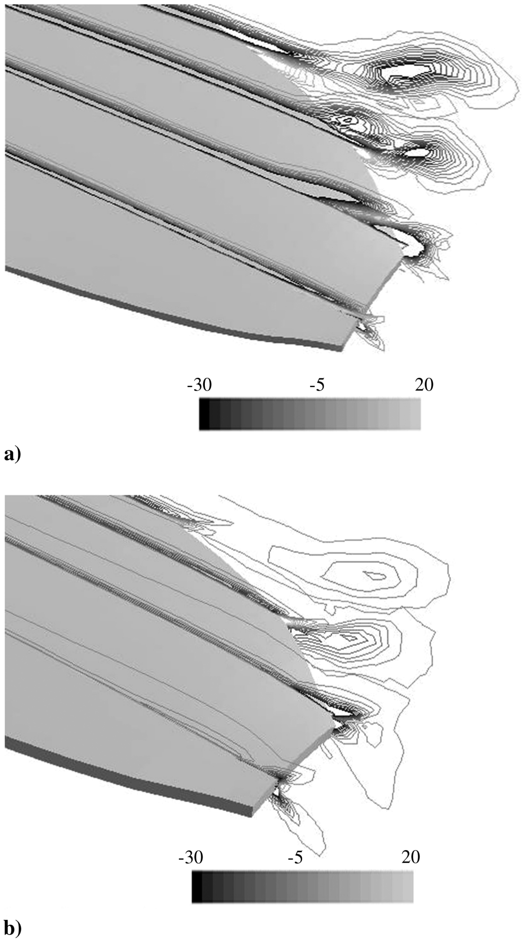

Fig. 12 Streamwise vorticity contours around upstream rotor tip: a) laminar model, and b) *k*-*ω* model.

balance were found to be 1.589 and 3.777%, respectively, contributing to the overall experimental errors. Other contributing factors to the errors are the balance-rotors installation and the differences of the rotor geometry used in the simulation and in the experiments which includes fabrication tolerances. Furthermore, the significantly low values for the torque, typically less than $1.00\mathrm{E}-03\ \mathrm{N}\cdot\mathrm{m}$, could result in significant interference with system noises further enhancing the experimental error. The values on the plots for zero Reynolds number are relative to the condition of power input to the upstream rotor and wind milling for the downstream rotor.

Figure 14 shows the experimental and calculated thrust versus Reynolds number based at the $3/4R$ of the downstream rotor at a rotors axial spacing of $1.07R$. The values include rotors total and single rotor thrusts and it was found that the thrust of upstream does not change significantly with Re number increase, which could be interpreted as the upstream rotor propulsive performance is not influenced by the downstream rotor. However, the performance of the downstream rotor is affected by the upstream rotor's wake resulting in a downstream rotor negative thrust at a very low Re numbers. The experimental study in [15] also showed the identical conclusion. Although simulations successfully predicted the trend, both upstream and downstream rotor thrusts are overestimated. Figure 15 shows the figures of merit (FM) of the upstream and downstream rotors versus the thrust coefficient to rotor solidity ratio from the simulations results. The maximum FM for the upstream rotor of 0.46 is higher than that of the downstream rotor (0.33). However, the best FMs for both rotors are significantly lower than typical full-scale rotors, which is in the range of 0.7–0.8. The lower FM are attributed to the low Reynolds number regime in which the nanorotor operates, inducing an important decrease of the kinetic energy of the blades laminar boundary layer causing a tendency of separation due to adverse pressure gradient thus causing a significant degradation in the static performance of coaxial nanorotor. It is also postulated that the counter-rotating motion of the rotors induces counter-rotating swirl flow induced by the upstream rotor resulting in a reduced FM of the downstream rotor.

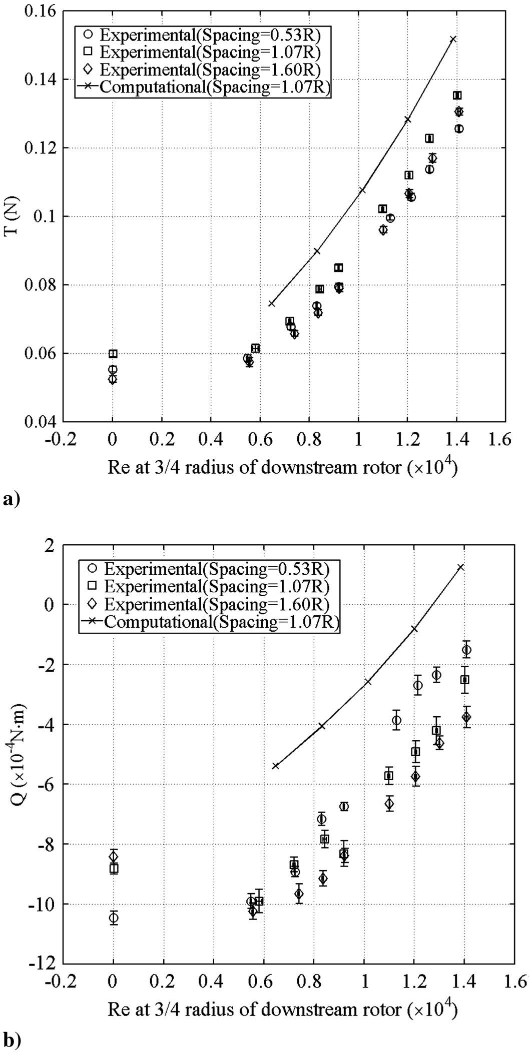

Fig. 13 Performance comparisons at different rotor axial spacing for: a) total thrust varying with *Re* number based at $\frac{3}{4}R$ of downstream rotor, and b) total torque.

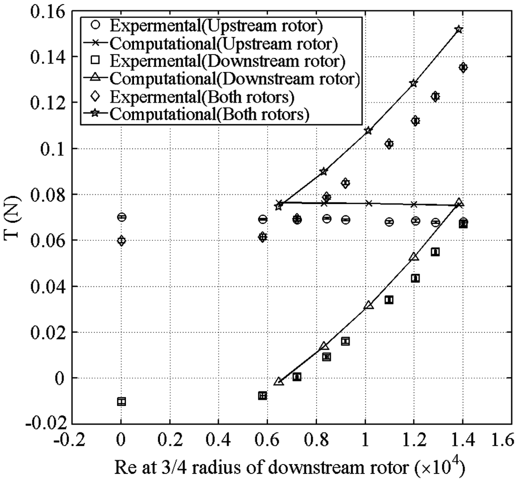

Fig. 14 Computational and experimental thrust of single upstream rotor, downstream rotor, and combined rotors at an axial spacing of 1.07*R*.

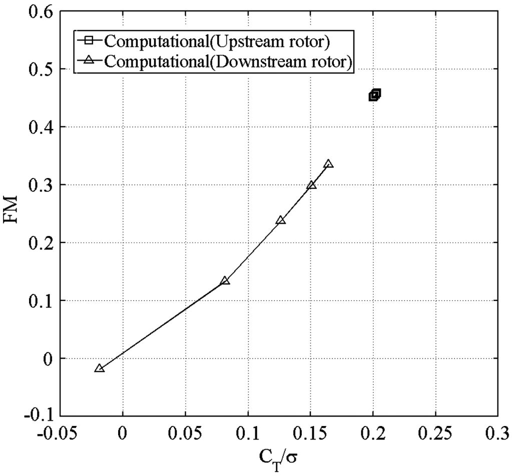

Fig. 15 Computational figure of merit versus thrust coefficient to rotor solidity ratio for rotors at an axial spacing of 1.07*R*.

V. Conclusions

The experimental and computational static performance of coaxial counter-rotating twin rotors with a diameter of 7.5 cm and twisted blades were studied using a novel 2 N maximum load five-component micro sting balance and FLUENT V6.3 software package. The experiments were performed at different rotor axial spacing to study their mutual interferences on the static performance. Before the experiments, the newly acquired sting balance was evaluated using a specifically designed 2 degree-of-freedom testing fixture, a high-resolution data acquisition system calibration check procedure. Several FLUENT simulations were performed applying different flow models including laminar model, S-A turbulence model, standard k-ω turbulence model, and k-ω SST turbulence model. Finally, coaxial rotor final simulations were run using the laminar fluid model and at a fixed upstream rotor rotational speed of 6500 RPM at various downstream rotor blade-tip speeds.

The sting balance validation tests showed average relative errors less than 4% for all components with excellent hysteresis characteristics. The rotors experimental and computational evaluations showed thrust values higher than 0.1 N with both rotors at 6500 RPM.

Both the experimental and computational results showed lower thrust and higher torque in respect to the values predicted from XROTOR. Furthermore, all flow models used in the FLUENT simulations overestimated the thrust and underestimated the torque, when compared with the experimental results. Laminar flow model captured better than standard k-ω turbulence model the disturbance of flowfield near the blade tip including the secondary vortices near the blade-tip and their merging with the main tip vortex structure. The comparison of experimental results obtained at constant tip speed and at different rotors axial spacing showed the highest thrust at a rotor's axial spacing of 1.07R. Experimental and computational thrust values versus the Reynolds number based at the 3/4 radius of the downstream rotor showed that the thrust of the upstream rotor does not significantly change increasing the Re number, which could be interpreted as the upstream rotor propulsive performance is not influenced by the downstream rotor. However, the performance of the downstream rotor was affected by the upstream rotor's wake resulting in a downstream rotor negative thrust at very low Re numbers. The figure of merit of the downstream rotor increased with the increase of the thrust coefficient to rotor solidity ratio, and the best figure of merit for the upstream rotor (0.46) was higher than the value for the downstream rotor (0.33).

Experiments with isolated rotor should be carried out to study the static performance of the single rotor and obtain a model validation. Improvements of the experimental setup should include higher resolution amplification equipment for the torque measurements. The simulations were performed with MRF method, therefore steady results were obtained. Unsteady methods such as the sliding mesh method or overset grids should be applied for an improved simulation of the tip vortex formation and evolution. Wind-tunnel tests should be carried out at different free stream velocities and angle of attack, including interference studies with a potential airframe.

Acknowledgments

The authors would like to thank the China Scholarship Council and the laboratory of the Department of Aerodynamics, Energetics and Propulsion, Institut Supérieur de l'Aéronautique et de l'Espace for the financial and facilities support. They would also like to thank Rémi Chanton, Guy Tessarotto, and Serge Gérard for help on the fabrication of test bench.

References

[1] Pines, D. J., and Bohorquez, F., "Challenges Facing Future Micro-Air-Vehicle Development," *Journal of Aircraft*, Vol. 43, No. 2, March–April 2006, pp. 290–305.
doi:10.2514/1.4922

[2] Grasmeyer, J. M., and Keennon, M. T., "Development of the Black Widow Micro Air Vehicle," *41st Aerospace Science Meeting Exhibit*, AIAA Paper 2001-0127, Jan. 2000.

[3] Bohorquez, F., Sirohi, S. P., Pines, D. J., and Rudd, L., "Design, Analysis and Hover Performance of a Rotary Wing Micro Air Vehicle," *Journal of the American Helicopter Society*, Vol. 48, No. 2, Jan. 2003, pp. 80–89.
doi:10.4050/JAHS.48.80

[4] Conn, A., Burgess, S., Hyde, R., and Ling, C. S., "From Natural Flyers to the Mechanical Realization of a Flapping Wing Micro Air Vehicle," *2006 IEEE International Conference on Robotics and Biomimetics*, IEEE Publications, Piscataway, NJ, 2006, pp. 439–444.
doi:10.1109/ROBIO.2006.340232

[5] *Proceedings of the 3rd US-European Competition and Workshop on Micro Air Vehicle and 7th European Micro Air Vehicle Conference and Flight Competition*, ONERA, Toulouse, France. 2007.

[6] Pines, D. J., "06-06 Proposer Information Pamphlet (PI) for Defense Advanced Research Project Agency (DARPA) Defense Sciences Office (DSO) Nano Air Vehicle (NAV) Program," DARPA DSO, Technical Rept. BAA 06-06, 2005.

[7] Youngren, H., Kroninger, C., Chang, M., and Jameson, S., "Low Reynolds Number Testing of the AG38 Airfoil for the SAMARAI Nano Air Vehicle," *46th AIAA Aerospace Sciences Meeting and Exhibit*, AIAA Paper 2008-417, Jan. 2008.

[8] Lesage, F., and Hamel, N., "Aerodynamic Study of a Flapping-Wing NAV Using a Combination of Numerical and Experimental Methods," *26th AIAA Applied Aerodynamics Conference*, AIAA Paper 2008-6396, Aug. 2008.

[9] He, R., and Sato, S., "Design of a Single-Motor Nano Aerial Vehicle with a Gearless Torque-Canceling Mechanism," *46th AIAA Aerospace Sciences Meeting and Exhibit*, AIAA Paper 2008-1417, Jan. 2008.

[10] Hein, B. R., and Chopra, I., "Hover Performance of a Micor Air Vehicle: Rotors at Low Reynolds Number," *Journal of the American Helicopter Society*, Vol. 52, No. 3, July 2007, pp. 254–262.
doi:10.4050/JAHS.52.254

[11] Tsuzuki, N., Sato, S., and Abe, T., "Design Guidelines of Rotary Wings in Hover for Insect-Scale Micro Air Vehicle Applications," *Journal of Aircraft*, Vol. 44, No. 1, Jan.–Feb. 2007, pp. 252–263.
doi:10.2514/1.23165

[12] Leishman, J. G., *Principles of Helicopter Aerodynamics*, 2nd ed., Cambridge Univ. Press, New York, 2006.

[13] Mueller, T. J., "Aerodynamic Measurements at Low Reynolds Numbers for Fixed Wing MAVs," Research and Technology Organization, von Karman Inst. for Fluid Dynamics, Belgium, 1999.

[14] Albertani, R., Hubner, P., Ifju, P., Lind, R., and Jackowski, J., "Wind Tunnel Testing of Micro Air Vehicles at Low Reynolds Numbers," *SAE 2004 Transactions: Journal of Aerospace*, Vol. 113, No. 1, 2005, pp. 1474–1486.
doi:10.4271/2004-01-3090

[15] Bohorquez, F., "Rotor Hover Performance and System Design of an Efficient Coaxial Rotary Wing Micro Air Vehicle," Ph.D. Dissertation, Aerospace Engineering Department, Univ. of Maryland, College Park, MD, 2007.

[16] Bohorquez, F., Pines, D., and Samuel, P. D., "Small Rotor Design Optimization Using Blade Element Momentum Theory and Hover Tests," *Journal of Aircraft*, Vol. 47, No. 1, Jan.–Feb. 2010, pp. 268–283.

doi:10.2514/1.45301

[17] Sato, S., Drela, M., Lang, J. H., and Otten, D. M., "Design and Characterization of Hover Nano Air Vehicle Propulsion System," *27th AIAA Applied Aerodynamics Conference*, AIAA Paper 2009-3962, June 2009.

[18] Deters, R. W., and Selig, M. S., "Static Testing of Micro Propellers," *26th AIAA Applied Aerodynamics Conference*, AIAA Paper 2008-6246, Aug. 2008.

[19] Schafroth, D., Bouabdallah, S., Bermes, C., and Siegwart, R., "From the Test Benches to the First Prototype of the muFly Micro Helicopter," *Journal of Intelligent and Robotic Systems*, Vol. 54, No. 1, June 2008, pp. 245–260.
doi:10.1007/s10846-008-9264-z

[20] Lakshminarayan, V. K., "Computational Investigation of Micro-Scale Coaxial Rotor Aerodynamics in Hover," Ph.D. Dissertation, Aerospace Engineering Department, Univ. of Maryland, College Park, MD, 2009.

[21] Modisette, J. M., and Darmofal, D. L., "An Output-based Adaptive and Higher-order Method for a Rotor in Hover," *26th AIAA Applied Aerodynamics Conference*, AIAA Paper 2008-6396, Aug. 2008.

[22] Strawn, R. C., and Djomehri, M. J., "Computational Modeling of Hovering Rotor and Wake Aerodynamics," *Journal of Aircraft*, Vol. 39, No. 5, Sept.–Oct. 2002, pp. 786–793.
doi:10.2514/2.3024

[23] Lakshminarayan, V. K., Bush, B. L., Duraisamy, K., and Baeder, J. D., "Computational Investigation of Micro Hovering Rotor Aerodynamics," *24th AIAA Applied Aerodynamics Conference*, AIAA Paper 2006-2819, June 2006.

[24] Schroeder, E. J., and Baeder, J. D., "Using Computational Fluid Dynamics for Micro-Air Vehicle Airfoil Validation and Prediction," *23rd AIAA Applied Aerodyanmics Conference*, AIAA Paper 2005-4814, June 2005.

[25] Lakshminarayan, V. K., and Baeder, J. D., "Computational Investigation of Small Scale Coaxial Rotor Aerodynamics in Hover," *47th AIAA Aerospace Sciences Meeting Including The New Horizons Forum and Aerospace Exposition*, AIAA Paper 2009-1069, Jan. 2009.

[26] Shyy, W., Lian, Y. S., Tang, J., Viieru, D., and Liu, H., *Low Re number Aerodynamics of Low Reynolds Number Flyers*, Cambridge Univ. Press, New York, 2008.

[27] Dietz, M., Kebler, M., Kramer, E., and Wagner, S., "Tip Vortex Conservation on a Helicopter Main Rotor Using Vortex-Adapted Chimera Grids," *AIAA Journal*, Vol. 45, No. 8, Aug. 2007, pp. 2062–2074.
doi:10.2514/1.28643

[28] Sitaraman, J., and Baeder, J. D., "Field Velocity Approach and Geometric Conservation Law for Unsteady Flow Simulations," *AIAA Journal*, Vol. 44, No. 9, Sept. 2006, pp. 2062–2074.
doi:10.2514/1.5836

[29] Steijl, R., and Barakos, G., "Sliding Mesh Algorithm for CFD Analysis of Helicopter Rotor-Fuselage Aerodynamics," *International Journal for Numerical Methods in Fluids*, Vol. 58, No. 5, Feb. 2008, pp. 527–549.
doi:10.1002/fld.1757

[30] Boelens, O. J., Van der ven, H., Oskam, B., and Hassan, A. A., "Boundary Conforming Disontinuous Galerkin Finite Element Approach for Rotorcraft Simulations," *Journal of Aircraft*, Vol. 39, No. 5, Sept.–Oct. 2002, pp. 776–785.
doi:10.2514/2.3023

[31] AIAA/GCTT, "Calibration and Use of Internal Strain-Gage Balances with Application to Wind Tunnel Testing," *AIAA Practices*, AIAA R-091-2003, 2003.

[32] Albertani, R., Khambatta, P., Hart, A., Ukeiley, L., Oyarzun, M., Cattafesta, L., and Abate, G., "Validation of a Low Reynolds Number Aerodynamic Characterization Facility," *47th AIAA Aerospace Sciences Meeting Including The New Horizons Forum and Aerospace Exposition*, AIAA Paper 2009-8805-8, Jan. 2009.

[33] Mastramico, D., and Hubner, J. P., "MC.-10-.375 Balance Evaluation Test," Technical Rept., Univ. of Alabama, Tuscaloosa, AL, 2006 (unpublished).

[34] Thipyopas, C., and Moschetta, J. M., "A Fixed-Wing Biplane MAV for Low Speed Missions," *International Journal of Micro Air Vehicles*, Vol. 1, No. 1, March 2009, pp. 13–34.
doi:10.1260/1756-8293.1.1.13

[35] Thipyopas, C., "Validation of Internal Micro Force Balance for Micro Air Vehicle Research," Rept. of Balance Verification, Institut Supérieur de l'Aéronautique et de l'Espace, July 2009 (unpublished).

[36] Ansys-Fluent, "Fluent 6.3 Documentation," Fluent Inc., Oct. 2006.

[37] MathWork Company, "Matlab & Simulink Student Version R2006a Manual," MathWork Company, Inc., 2006.

[38] Larrabee, E. E., "Practical Design of Minimum Induced Loss Propellers," SAE Paper 790585, Society of Automotive Engineers, 1979.

[39] Adkins, C. N., "Design of Optimum Propellers," *Journal of Propulsion and Power*, Vol. 10, No. 5, Sept–Oct. 1994, pp. 676–682.
doi:10.2514/3.23779

[40] Liu, Z., "Résumé de l'Experience," Rept. of Thesis, Institut Supérieur de l'Aéronautique et de l'Espace, Toulouse, France, Aug. 2008.

[41] Drela, M., and Youngren, H., "Xrotor User Guide," Massachusetts Inst. of Technology, Cambridge, MA, 2002.